Energy Transfer, Discontinuities, and Heating in the Inner Heliosphere Measured with a Weak and Local Formulation of the Politano–Pouquet Law

V. David, S. Galtier, Fouad Sahraoui, L. Z. Hadid

The Astrophysical Journal, 927:200 (10pp), 2022 March 10 https://doi.org/10.3847/1538-4357/ac524b

Energy Transfer, Discontinuities, and Heating in the Inner Heliosphere Measured with a Weak and Local Formulation of the Politano–Pouquet Law

V. David[1], S. Galtier[1,2], F. Sahraoui[1], and L. Z. Hadid[1]
[1] Laboratoire de Physique des Plasmas (LPP), Université Paris-Saclay, CNRS, École Polytechnique, Institut Polytechnique de Paris, Sorbonne Université, Observatoire de Paris, F-91120 Palaiseau, France
[2] Institut Universitaire de France, Paris, France
Received 2021 November 25; revised 2022 February 2; accepted 2022 February 3; published 2022 March 17

Abstract

The solar wind is a highly turbulent plasma for which the mean rate of energy transfer ε has been measured for a long time using the Politano–Pouquet (PP98) exact law. However, this law assumes statistical homogeneity that can be violated by the presence of discontinuities. Here, we introduce a new method based on the inertial dissipation $\mathcal{D}_{\rm I}^{\sigma}$ whose analytical form is derived from incompressible magnetohydrodynamics; it can be considered as a weak and *local* (in space) formulation of the PP98 law whose expression is recovered after integration in space. We used $\mathcal{D}_{\rm I}^{\sigma}$ to estimate the local energy transfer rate at scale σ from the THEMIS-B and Parker Solar Probe data taken in the solar wind at different heliospheric distances. Our study reveals that discontinuities near the Sun lead to a strong energy transfer that affects a wide range of scales σ. We also observe that switchbacks seem to be characterized by a singular behavior with an energy transfer varying as $\sigma^{-3/4}$, which slightly differs from classical discontinuities characterized by a σ^{-1} scaling. A comparison between the measurements of ε and $\mathcal{D}_{\rm I}^{\sigma}$ shows that in general the latter is significantly larger than the former.

Unified Astronomy Thesaurus concepts: Interplanetary turbulence (830); Space plasmas (1544); Solar wind (1534)

1. Introduction

For several decades, the solar wind—a collisionless plasma—has been the subject of an apparent paradox. The measurements made by Voyager 1 and 2 revealed that the average (proton) temperature of the solar wind decreases as $\sim r^{-0.5}$ over 1–20 astronomical units (au), with r, the radial distance from the Sun (Gazis & Lazarus 1982; Marsch et al. 1982; Richardson et al. 1995; Matthaeus et al. 1999). However, for a radially expanding, adiabatically cooling plasma, one would expect a temperature variation as $r^{-4/3}$, which is significantly steeper than the observed law. This paradox can be solved if an efficient local heating source exists, which must be collisionless in nature (note, however, that the adiabatic model can be questioned since it derives from a fluid approximation, which implicitly assumes the existence of collisions).

In the heliosphere at intermediate radial distances ($r \gtrsim 2$ au) turbulence generated by stream shears or large-scale shocks at the interface between high and low speed streams was quickly suspected as a major source of heating (Gazis & Lazarus 1982; Burlaga & Mish 1987; David & Galtier 2021). In the far outer solar wind ($r > 20$ au) where the temperature increases slightly (Matthaeus et al. 1999; Elliott et al. 2019), pickup ions are considered a main source of heating (Gazis et al. 1994; Pine et al. 2020a). Originally, these are neutrals from the interstellar medium that are transformed into ions by charge exchange with solar wind protons, that are eventually picked up by the interplanetary magnetic field. In this context, several (phenomenological) turbulence transport model equations have been successfully used to study the solar wind heating (Zank et al. 1996, 2018).

In the inner heliosphere ($r \lesssim 1$ au), the wind is generally free from large-scale structures such as the interplanetary shocks observed at 5 au, and turbulent fluctuations are dominant. Therefore, studies focus on the turbulent cascade which is seen as an efficient mechanism to bring energy from large magnetohydrodynamic (MHD) scales to small kinetic (sub-MHD) ones (Sahraoui et al. 2020). In situ measurements of ε, the mean rate of energy transfer at MHD scales, provide an estimate of the heating rate by assuming complete conversion from the former to the latter. While those estimates cannot inform us about the precise kinetic mechanism responsible for energy dissipation, recent progress using Landau-fluid simulations showed the ability of the exact laws to estimate the amount of dissipation, due to Landau damping (Ferrand et al. 2021).

In practice, ε can be estimated from exact laws. First developed in incompressible hydrodynamics (Kolmogorov 1941; Batchelor 1953; Antonia et al. 1997), the exact laws have been derived for many physical systems where turbulence is encountered. This includes isothermal compressible hydrodynamics (Galtier & Banerjee 2011), a model often used to simulate supersonic interstellar turbulence (Kritsuk et al. 2007; Federrath et al. 2010; Ferrand et al. 2020). For the solar wind, the simplest exact law is that derived from incompressible MHD (Politano & Pouquet 1998). Its use led to the first estimate of turbulent heating in the solar wind (Sorriso-Valvo et al. 2007; MacBride et al. 2008; Marino et al. 2008; Stawarz et al. 2009, 2010; Osman et al. 2011). Later, several generalized exact laws were derived to account for compressible MHD (Banerjee & Galtier 2013; Andrés & Sahraoui 2017; Simon & Sahraoui 2021), Hall-MHD (Galtier 2008; Banerjee & Galtier 2016; Andrés et al. 2018; Hellinger et al. 2018; Ferrand et al. 2021), and even gravitoturbulence (Banerjee & Kritsuk 2017, 2018). With these new laws, it was possible to obtain better estimates of ε in the solar wind and planetary plasma environments that incorporate density fluctuations and subion

scale effects (Banerjee et al. 2016; Hadid et al. 2017; Andrés et al. 2019; Bandyopadhyay et al. 2020; Andrés et al. 2021).

Exact laws are based on the zeroth law of turbulence (unproved in general), which says that in a turbulence experiment, everything else being fixed, if the energy dissipation ends to zero, the mean rate of energy dissipation tends to a nonzero limit, which is ε (Frisch 1995). This law has led to an interesting mathematical development around the concept of weak solutions in Euler's equation, useful when the velocity becomes nonregular (Leray 1934). In particular, the nonregularity of the field can lead, in principle, to energy dissipation without the assistance of viscosity (Onsager 1949). This new form of dissipation has been called inertial dissipation (noted hereafter as $\mathcal{D}_I$) as opposed to viscous dissipation. The mathematical expression of $\mathcal{D}_I$ for the Euler equation (Duchon & Robert 2000) has a striking similarity with Kolmogorov's law (Antonia et al. 1997). Unlike the exact law, the expression of $\mathcal{D}_I$ does not involve an ensemble average; therefore, it can be used at any point in a turbulent fluid to evaluate the local (in space) dissipation (Saw et al. 2016). This work on incompressible hydrodynamics has recently been generalized to 3D incompressible Hall-MHD (Galtier 2018) and to a 1.5D MHD system (Yanase 1997) that has been used to estimate the inertial dissipation produced by collisionless shocks in the outer heliosphere (David & Galtier 2021). As with Burgers' equation (Dubrulle 2019; Eyink 2019), with the low dimensional MHD model, the zeroth law of turbulence can be proved with, on average, $\langle \mathcal{D}_I \rangle = \varepsilon$.

The structure of the paper is as follows: Section 2 is devoted to theoretical frameworks (incompressible MHD, exact law, inertial dissipation). Section 3 presents the selection of data (THEMIS-B; Parker Solar Probe, hereafter PSP) and their processing; various situations are considered (slow and fast winds, discontinuities). The results of our analysis are presented in Section 4 with the measurements of ε and $\mathcal{D}_I$, in particular. A conclusion is provided in Section 5.

2. MHD Theory

2.1. Four-thirds Exact Law

We briefly recall the four-thirds exact law for incompressible MHD derived by Politano & Pouquet (1998), which we will hereafter call the PP98 law. Let $\boldsymbol{u}$ be the fluid velocity, $\boldsymbol{b} \equiv \boldsymbol{B}/\sqrt{\mu_0 \rho_0}$ the magnetic field normalized to a velocity, with ρ_0 the mean plasma density and μ_0 the vacuum permeability, $P_* = P + b^2/2$ the sum of the thermal and magnetic pressures, ν the kinematic viscosity, and η the magnetic diffusivity. Then, the incompressible MHD equations read (Galtier 2016):

$$\partial_t \boldsymbol{u} + \boldsymbol{u} \cdot \nabla \boldsymbol{u} = -\nabla P_* + \boldsymbol{b} \cdot \nabla \boldsymbol{b} + \nu \nabla^2 \boldsymbol{u}, \tag{1}$$

$$\partial_t \boldsymbol{b} + \boldsymbol{u} \cdot \nabla \boldsymbol{b} = \boldsymbol{b} \cdot \nabla \boldsymbol{u} + \eta \nabla^2 \boldsymbol{b}, \tag{2}$$

where $\boldsymbol{u}$ and $\boldsymbol{b}$ are zero-divergence fields. To derive these equations, the following Ohm's law is used:

$$\boldsymbol{e} = \eta \boldsymbol{j} - \boldsymbol{u} \times \boldsymbol{b}, \tag{3}$$

where $\boldsymbol{e}$ is the normalized electric field and $\boldsymbol{j} = \nabla \times \boldsymbol{b}$ is the normalized electric current density. To obtain the PP98 law, we assume large-scale stationary forcing and asymptotically large (magnetic and kinetic) Reynolds numbers. After a standard calculation, one obtains a primitive form of the PP98 exact law:

$$-4\varepsilon = \nabla_\ell \cdot \langle (|\delta \boldsymbol{u}|^2 + |\delta \boldsymbol{b}|^2) \delta \boldsymbol{u} - 2(\delta \boldsymbol{u} \cdot \delta \boldsymbol{b}) \delta \boldsymbol{b} \rangle, \tag{4}$$

where $\langle \cdot \rangle$ is the ensemble average. For any variable g, $\delta g \equiv g(\boldsymbol{x} + \boldsymbol{\ell}) - g(\boldsymbol{x})$, with $\boldsymbol{\ell}$ the vector increment. In this equation, ε is the mean rate of energy transfer/dissipation/forcing, the equivalence between the three definitions being due to the stationarity assumption.

The previous expression can be reduced to the PP98 law when the statistical isotropy is further assumed:

$$-\frac{4}{3}\varepsilon \ell = \langle (|\delta \boldsymbol{u}|^2 + |\delta \boldsymbol{b}|^2) \delta u_\ell - 2(\delta \boldsymbol{u} \cdot \delta \boldsymbol{b}) \delta b_\ell \rangle. \tag{5}$$

Here, the index ℓ refers to a projection along the longitudinal direction given by the vector $\boldsymbol{\ell}$, with ℓ as its norm. The PP98 exact law is valid in the inertial range of incompressible MHD turbulence. A basic assumption made to use the law (5) is that the fields are regular. In simple terms, a field is said to be regular if all the classical tools of analysis (such as derivative calculations) can be applied. In case of nonregular fields (e.g., a discontinuity), a weak formulation must be introduced.

2.2. Weak Formulation

The weak formalism is based on smoothing of a field with some kernel $\varphi \in \mathbb{C}^\infty$ with compact support on $\mathbb{R}^3$, even nonnegative, and with integral 1. To formalize the notion of scale, we define a family of test functions[3] φ^σ such that $\varphi^\sigma(\boldsymbol{\xi}) \equiv \sigma^{-3} \varphi(\boldsymbol{\xi}/\sigma)$. The regularized fields at scale σ are defined by taking the convolution product of the fields with φ^σ (for simplicity, the time dependence is omitted):

$$\boldsymbol{u}^\sigma(\boldsymbol{x}) \equiv \varphi^\sigma * \boldsymbol{u} = \int_{\mathbb{R}^3} \varphi^\sigma(\boldsymbol{\xi}) \boldsymbol{u}(\boldsymbol{x} + \boldsymbol{\xi}) \mathrm{d}\boldsymbol{\xi}, \tag{6}$$

which tends to $\boldsymbol{u}(\boldsymbol{x})$ when $\sigma \to 0$. The other regularized quantities are defined in the same way. Note that this filtering process consists of smoothing the fields in a space defined by a sphere of radius σ centered at the point $\boldsymbol{\xi}$ (see Figure 1). Under these considerations, the kinetic energy reads

$$E_u^\sigma(\boldsymbol{x}) \equiv \frac{1}{2} u_i u_i^\sigma = \frac{1}{2} \int_{\mathbb{R}^3} \varphi^\sigma(\boldsymbol{\xi}) u_i(\boldsymbol{x}) u_i(\boldsymbol{x} + \boldsymbol{\xi}) \mathrm{d}\boldsymbol{\xi}, \tag{7}$$

where the Einstein summation convention is used (the generalization to the magnetic energy is straightforward). The previous equation can also be interpreted as the local equivalent of a correlation function where the ensemble average is replaced by a local average over scale.

With the above definitions and using a point-splitting regularization, one can derive the following weak formulation (valid for individual realizations) of the local energy conservation at position $\boldsymbol{x}$ (Galtier 2018):

$$\partial_t E^\sigma(\boldsymbol{x}) + \nabla \cdot \boldsymbol{\Pi}^\sigma(\boldsymbol{x}) = -\mathcal{D}^\sigma_{\nu,\eta}(\boldsymbol{x}) - \mathcal{D}^\sigma_I(\boldsymbol{x}), \tag{8}$$

with $E^\sigma = E_u^\sigma + E_b^\sigma$ the total energy. $\boldsymbol{\Pi}^\sigma$ is the spatial flux whose heavy form is not given explicitly here; this is a purely local term that describes how energy is transported across the

[3] There is no unique solution for the test function. However, with this definition, the inertial dissipation does not depend on the test function in the limit $\sigma \to 0$ because in this case the test function tends to a Dirac (Duchon & Robert 2000).

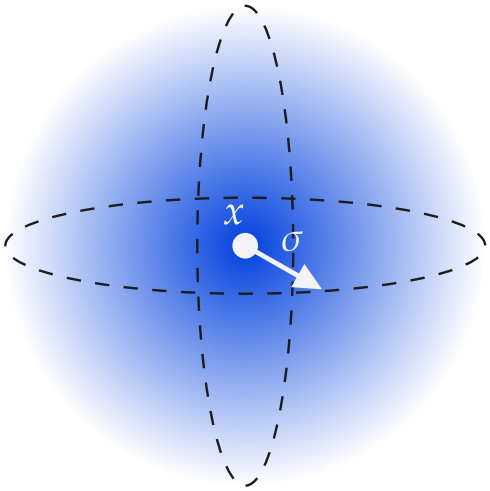

Figure 1. Scheme of the filtering process. The color reflects the intensity of the smoothing. σ can be seen as the typical scale beyond which the contribution to the integral (see Equation (6)) is mainly negligible.

flow, and it vanishes after integration over space with the appropriate boundary conditions. We also have the energy dissipation by viscous and resistive effects (that includes the vorticity $\boldsymbol{\omega} = \nabla \times \boldsymbol{u}$),

$$\mathcal{D}^{\sigma}_{\nu,\eta}(\boldsymbol{x}) = \nu\boldsymbol{\omega}\cdot\boldsymbol{\omega}^{\sigma} + \eta\boldsymbol{j}\cdot\boldsymbol{j}^{\sigma}, \tag{9}$$

and the inertial (also called anomalous or defect; Eyink 2003) dissipation,

$$\mathcal{D}^{\sigma}_{\mathrm{I}}(\boldsymbol{x}) = \frac{1}{4}\int_{\mathbb{R}^3} \nabla\varphi^{\sigma}(\boldsymbol{\xi})\cdot\boldsymbol{Y}(\boldsymbol{x},\boldsymbol{\xi})\mathrm{d}\boldsymbol{\xi}, \tag{10}$$

where the third-order mixed structure function reads

$$\boldsymbol{Y}(\boldsymbol{x},\boldsymbol{\xi}) = (|\delta\boldsymbol{u}|^2 + |\delta\boldsymbol{b}|^2)\delta\boldsymbol{u} - 2(\delta\boldsymbol{u}\cdot\delta\boldsymbol{b})\delta\boldsymbol{b}, \tag{11}$$

with $\delta g \equiv g(\boldsymbol{x}+\boldsymbol{\xi}) - g(\boldsymbol{x})$. Equation (8) must be seen as a generalization of the PP98 law (or more precisely of the Kármán-Howarth MHD equation; Politano & Pouquet 1998) that we can recover for regular fields and homogeneous turbulence (see below). Note that in the limit $\sigma \to 0$, the two dissipative terms are mutually exclusive; the presence of any viscosity/resistivity should prevent the formation of singularities. Thus, in this limit, only one of them can appear in the equation. Another physical relevance of the weak formulation is revealed when performing an integration over space. The absence of an energy source at the boundary is formally equivalent to assuming periodicity (or homogeneity); therefore, the notation $\langle\cdot\rangle$ will be used for integration in space. We find

$$\partial_t\langle E^{\sigma}\rangle = -\langle\mathcal{D}^{\sigma}_{\nu,\eta}\rangle - \langle\mathcal{D}^{\sigma}_{\mathrm{I}}\rangle, \tag{12}$$

with

$$\langle\mathcal{D}^{\sigma}_{\mathrm{I}}\rangle = \frac{1}{4}\int_{\mathbb{R}^3}\nabla\varphi^{\sigma}(\boldsymbol{\xi})\cdot\langle\boldsymbol{Y}(\boldsymbol{x},\boldsymbol{\xi})\rangle\mathrm{d}\boldsymbol{\xi}. \tag{13}$$

In the small-scale limit, we find for a viscous/resistive flow

$$\lim_{\sigma\to 0}\langle\mathcal{D}^{\sigma}_{\nu,\eta}\rangle \equiv \langle\mathcal{D}_{\nu,\eta}\rangle = \varepsilon. \tag{14}$$

Therefore, $\mathcal{D}^{\sigma}_{\nu,\eta}$ can be used to trace, locally and across scales, the rate of viscous/resistive energy dissipation (Kuzzay et al. 2019). On the other hand, Equation (13) has a strong similarity

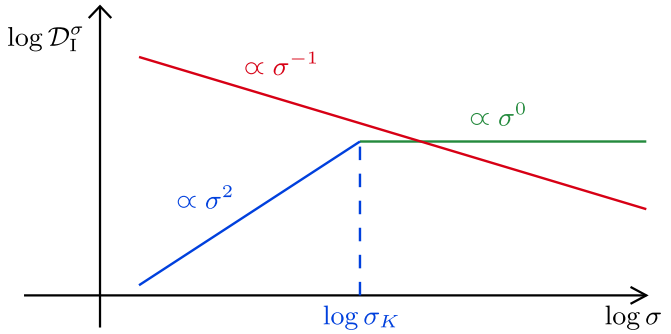

Figure 2. Variation (schematic) of the inertial dissipation $\mathcal{D}^{\sigma}_{\mathrm{I}}(\boldsymbol{x})$ as a function of the scale σ for a discontinuity (red line), turbulent fluctuations (green line), and viscous/resistive damping (blue line). The intersection between the green and the blue lines defines the dissipative (i.e., Kolmogorov) scale and is noted σ_K. Similarly, the intersection between the green and the red line can define the discontinuity scale below which discontinuities become dominant (see Figure 4).

with the right-hand side term of the exact law (4), especially if one performs an integration by part, assuming the fields to be regular, and takes the small-scale limit

$$\begin{aligned}\mathcal{D}_{\mathrm{I}}(\boldsymbol{x}) &\equiv \lim_{\sigma\to 0}\mathcal{D}^{\sigma}_{\mathrm{I}}(\boldsymbol{x})\\ &= -\lim_{\sigma\to 0}\frac{1}{4}\int_{\mathbb{R}^3}\varphi^{\sigma}(\boldsymbol{\xi})\nabla\cdot\boldsymbol{Y}(\boldsymbol{x},\boldsymbol{\xi})\mathrm{d}\boldsymbol{\xi}.\end{aligned} \tag{15}$$

This relation directly connects $\mathcal{D}_{\mathrm{I}}$ to the PP98 law, which leads to the remarkable equality $\langle\mathcal{D}_{\mathrm{I}}\rangle = \varepsilon$ (see Appendix A). Therefore, $\mathcal{D}^{\sigma}_{\mathrm{I}}$ can be used to trace, locally and across scales, the rate of energy transfer.

Other interpretations can be made based on Equation (15). In the presence of finite viscosity and resistivity, the fields are regular (because the Laplacian operator smooths the fields at small scales) and thus satisfy $\lim_{\xi\to 0^+}\delta\boldsymbol{u} = \lim_{\xi\to 0^+}\delta\boldsymbol{b} = 0$, which leads to $\mathcal{D}_{\mathrm{I}} = 0$; this is the classical situation. On the contrary, if $\nu = \eta = 0$, nonregular fields can be produced and $\mathcal{D}_{\mathrm{I}}$ can have a contribution. This contribution, however, is not systematic because the fields must satisfy the Hölder condition (Onsager 1949; Dubrulle 2019). Using a scaling analysis (at a fixed position $\boldsymbol{x}$), we can make three theoretical predictions of practical importance:

1. In the inertial range where the fields correspond to turbulent fluctuations that obey the PP98 law in the inertial range, we have[4] $\delta u^3 \sim \delta b^3 \sim \sigma$ and thus $\mathcal{D}^{\sigma}_{\mathrm{I}}(\boldsymbol{x}) \sim \sigma^0$.
2. At small scales where viscous/resistive effects dominate, a Taylor expansion gives $\delta u \sim \delta b \sim \sigma$ and thus $\mathcal{D}^{\sigma}_{\mathrm{I}}(\boldsymbol{x}) \sim \sigma^2$.
3. However, when the fields are nonregular and act like discontinuities, the increments correspond to jumps $\delta u \sim \Delta_u$, $\delta b \sim \Delta_b$ and thus $\mathcal{D}^{\sigma}_{\mathrm{I}}(\boldsymbol{x}) \sim \sigma^{-1}$.

Therefore, depending on the scaling that would be measured in the solar wind (see below) it will be possible to make a distinction between turbulence, viscous/resistive damping, and discontinuities (see Figure 2). Note, however, that other σ dependences are possible for nonregular fields (Jaffard 2006; Lashermes et al. 2008; Jaffard et al. 2009).

To conclude, we point out that $\mathcal{D}_{\mathrm{I}}$ is a generalized function (i.e., a distribution) and its analytic form (if it can be found) can lead to the appearance of a δ-function (see, e.g., David &

[4] We do not mean equipartition between kinetic and magnetic energies, but only the same σ dependence.

Galtier 2021). This means that when the limit $\sigma \to 0$ is taken, one expects to see the value of $|\mathcal{D}_I^\sigma|$ increase without limit; however, in practice, the value $\sigma = 0$ will never be reached (see below).

3. Methods

3.1. Data Selection

In a first step, we used the THEMIS-B/ARTEMIS P1 spacecraft data during time intervals when it was traveling in the free-streaming solar wind. The magnetic field data and plasma moments (proton density and velocity) were measured respectively by the Fluxgate Magnetometer (MAG) and the Electrostatic Analyzer. All data are expressed in the Geocentric Solar Ecliptic (GSE) coordinate system, and have a time resolution $dt = 3$ s, which corresponds to the spacecraft spin period. We analyzed more than 180 hr of data between 2008 and 2011 that cover both fast and slow solar winds. Fast winds are defined as having an average speed $U_{SW} > 450$ km s^{-1}. The others are the slow winds.

In a second step, we analyze PSP's data measured between 2018 and 2020 during the first and fifth approaches of the spacecraft to the Sun. We selected two subsets with a total duration of about 115 hr, corresponding roughly to radial distances of 36 and 30 solar radii (at perihelion) to which we refer respectively by subsets PSP1 and PSP5. The magnetic field and plasma moments (proton density and velocity) were measured respectively by the MAG and the Solar Probe Analyzer (SPAN). All data are expressed in the Radial Tangential Normal (RTN) coordinate system, and have a time resolution $dt = 1$s.

3.2. Data Processing

For both spacecraft, the selected intervals are divided into samples of 2 hr, which correspond to a number of data points, $N = 2400$ for THEMIS-B and $N = 7200$ for PSP. The data selection yielded the following:

1. 51 samples (122,400 data points) in the slow solar wind.
2. 46 samples (110,400 data points) in the fast solar wind.
3. 61 samples (439,200 data points) for PSP1.
4. 55 samples (396,000 data points) for PSP5.

Data gaps (rarely present) were interpolated linearly. For the selected time intervals, we compute the energy cascade rates ε estimated by PP98 and the inertial dissipation $\mathcal{D}_I^\sigma$ using Equations (5) and (10), respectively. The structure functions of $\boldsymbol{u}$ and $\boldsymbol{b}$ are calculated for different time lags $\tau \in [1, 100]dt$ to probe the scales of the inertial range. As usual (see, e.g., Hadid et al. 2017), we use the Taylor hypothesis $\tau = -\xi/U_{SW}$, with U_{SW} the mean solar wind speed on the interval, assuming that $\mathcal{D}_I = \mathcal{D}_I^{\sigma_{min}}$, with σ_{min} the minimum accessible value, which is 3 s for THEMIS-B and 1 s for PSP data. We note $\langle \mathcal{D}_I^\sigma \rangle$ the time average of the inertial dissipation over the 2 hr sample.

Mathematically, the inertial dissipation $\mathcal{D}_I^\sigma$ can be interpreted as a continuous wavelet transform of the third-order structure function $\boldsymbol{Y}$ with respect to the wavelet φ. The link between the weak formulation and the wavelet transform reveals several advantages of its application to rough turbulent fields. Indeed, a wavelet transform can be considered as a "local Fourier transform" and it is suitable for application to inhomogeneous fields. Thus, it will genuinely deal with the observed breaking of the spatial translation symmetry (Dubrulle 2019). Therefore, we computed $\mathcal{D}_I^\sigma$ on the entire time interval for 100 values of σ as a continuous 1D wavelet transform based on fast Fourier transform—a MATLAB package provided by the toolbox YAWTB (Jacques et al. 2010). The test function φ^σ is a normalized Gaussian of width σ, which is convenient because its derivative is exact (more information on the different ways to implement $\mathcal{D}_I$ is given in Appendix A). Note that in the implementation of the inertial dissipation, only the terms depending on ξ are computed because the convolution product is performed on this variable and, given the properties of φ^σ, it is obvious that the smoothing of a field independent of ξ leaves the result unchanged. To minimize the finite window size effects due to the nonperiodicity of the data, we artificially extend each time series to twice its size to apply a Gaussian windowing prior to computing its Fourier transform. The final result is obtained in the time domain after an inverse Fourier transform where only the information from the central part of the time series (i.e., the original one of interest) is considered.

4. Observational Results

4.1. Inhomogeneous Structures

We begin our data analysis with four examples where discontinuities are clearly present. In Figure 3 we show (top left) a THEMIS-B slow wind interval on 2008 August 8 from 02:54:36 to 04:54:36, (top right) a THEMIS-B fast wind interval on 2011 April 4 from 21:15:23 to 23:15:23, (bottom left) a PSP1 interval on 2018 November 6 from 09:00:00 to 11:00:00, and (bottom right) a PSP5 interval on 2020 June 3 from 22:00:00 to June 4, 00:00:00. For each case study, the first two panels (top to bottom) show the three components of the proton velocity and the magnetic field, respectively. They highlight the presence of discontinuities, and thus the breaking of statistical homogeneity, which may jeopardize the use of exact laws. We find that for the PSP intervals that are closer to the Sun, the velocity and magnetic field components are strongly correlated (respectively 91%, 90%, and 91% for the radial, tangential, and normal components for the PSP1 interval, and 96%, 86%, and 80% for the PSP5 one), which can be interpreted as the signature of outward propagating Alfvén waves (Belcher & Davis 1971). The third panel shows the proton density, which is relatively constant, and the last panel shows a space-scale diagram of the inertial dissipation (in modulus); time is on the x-axis, the width σ of the test function is on the y-axis, and the intensity of $|\mathcal{D}_I^\sigma|$ is in color. These maps illustrate the local energy transfer between different scales σ (at a given time t, or using the Taylor hypothesis, at a given position $x = -U_{SW}t$ with U_{SW} the solar wind speed). If we follow the evolution of the plasma from small to large scales, the dark areas delimit the impact of an event on the energy transfer; the larger the bright area in scale, the greater the impact of the event in scale, and the smaller the local energy transfer would be. Conversely, when a region is mainly dark, this means that the energy transfer is local and the dynamics is driven by turbulent fluctuations.

A more precise analysis can be made by observing how $|\mathcal{D}_I^\sigma|$ evolves according to the scale σ at given times $t_\star$ and t_f. We respectively chose $t_\star$ and t_f such that $|\mathcal{D}_I(t_\star)| = \max(|\mathcal{D}_I|)$ and $|\mathcal{D}_I^\sigma(t_f)| = \min(|\mathcal{D}_I|)$ over the 2 hr interval (see Figure 3). The first and second panels of Figure 4 reveal that, when placed respectively on a discontinuity (at time $t_\star$) and on a turbulent fluctuation (at time t_f), the inertial dissipation does follow the σ^{-1} and σ^0 power laws, as theoretically expected. The third

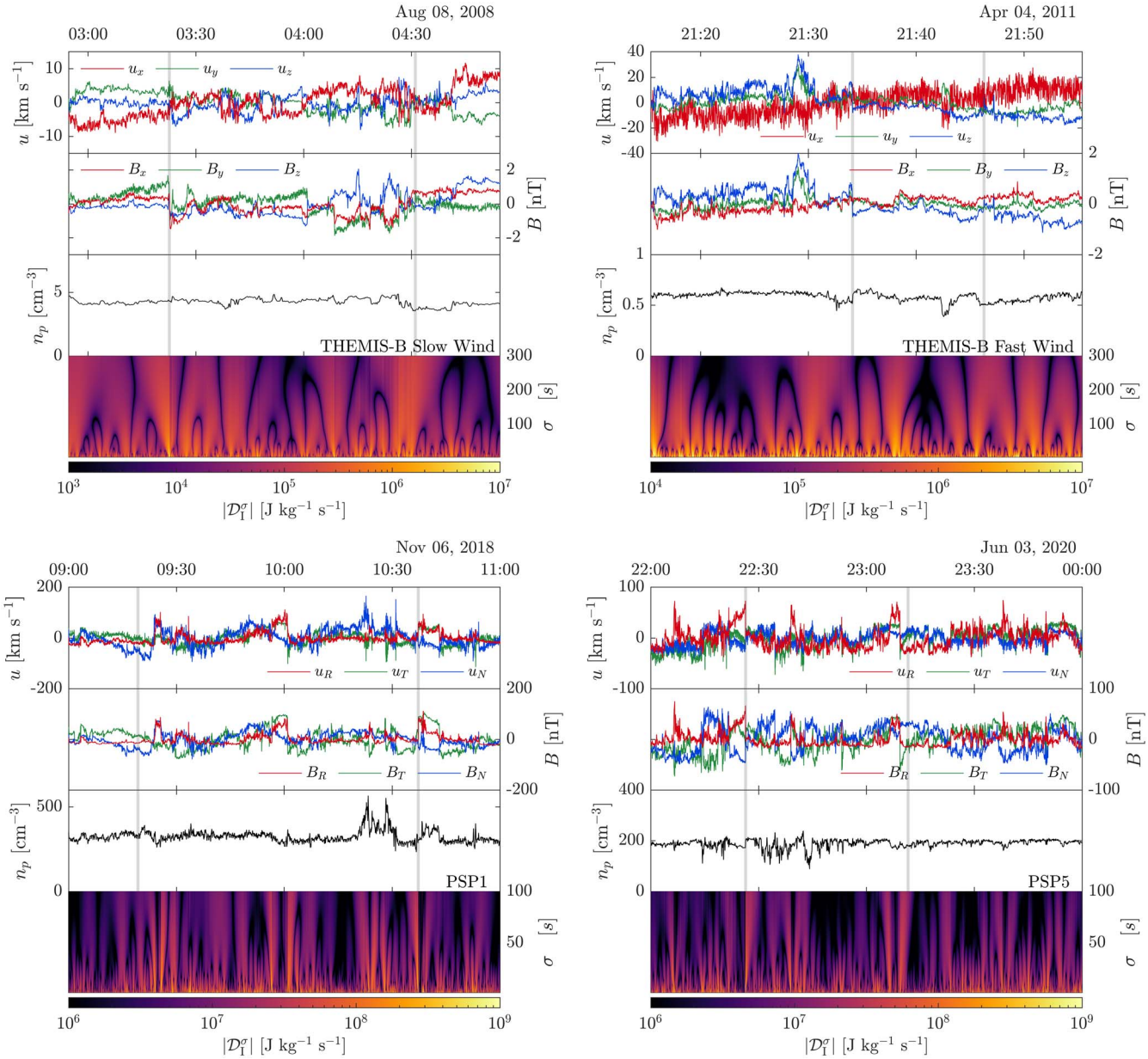

Figure 3. Top panels display the slow (left) and fast (right) winds measured with THEMIS-B. Bottom panels display PSP1 (left) and PSP5 (right). In each panel, from top to bottom, we find the fluctuations of the velocity components, fluctuations of the magnetic field components, proton density, and space-scale diagram (in modulus) of the inertial dissipation. The red, blue, and green curves correspond respectively to the x, y, z components (GSE coordinates) for THEMIS-B and to the R, T, N components (RTN coordinates) for PSP. The vertical gray lines locate the instant for which $|\mathcal{D}_I|$ is extremal on the sample.

panel shows the evolution of the inertial dissipation $|\langle\mathcal{D}_I^\sigma\rangle|$, averaged over the entire intervals of 2 hr, as a function of σ. The power laws that were found indicate the dominant type of energy transfer. For those coming from THEMIS-B (in blue), we observe mainly a flat profile, which means that the dominant mechanism is a turbulent cascade, due to fluctuations. For PSP1 (light red), a power law in σ^{-1} appears at small σ, showing the prevalence of discontinuities at small scales for this interval. For PSP5 (dark red), an intermediate power law is observed suggesting that the effect of discontinuities is weaker. The bottom panel displays the value of $|\varepsilon|$ as a function of τ for the four intervals. We can see that the curves do not exhibit a clear plateau as theoretically expected; this might be due to the violation of one (or more) of the assumptions on which the exact law formalism is grounded. This is particularly the case for the statistical homogeneity, which is unlikely to be valid here because of the presence of discontinuities that distort the estimate of the mean rate of energy cascade (Hadid et al. 2017). Note that for the PSP intervals close to the Sun, both intervals give the same order of magnitude of the inertial dissipation, but are larger than that from THEMIS data at 1 au, which, overall, remains true for the other intervals. This is consistent with the the radial increase of the turbulent cascade rate ε as one approaches the Sun (Bandyopadhyay et al. 2020; Andrés et al. 2021). Also the inertial dissipation is larger for fast than for slow solar winds in agreement with previous results regarding the cascade rate ε (Hadid et al. 2017).

4.2. Switchbacks

Switchbacks are defined as sudden reversals of the radial magnetic field component associated with sharp variations in the

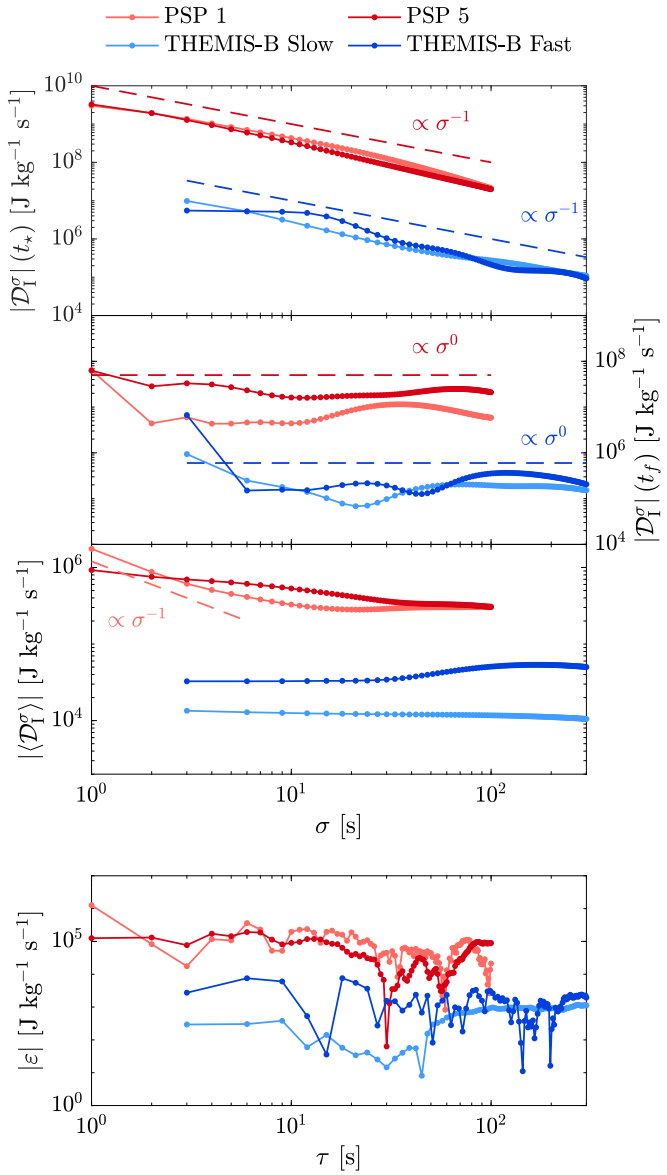

Figure 4. From top to bottom: modulus of the inertial dissipation at time $t_\star$ as a function of scale σ, modulus of the inertial dissipation at time t_f as a function of scale σ, estimates of the mean inertial dissipation as a function of σ, and modulus of the mean rate of energy cascade as a function of τ. Here, σ and τ vary approximately on the same interval.

radial plasma flow (Neugebauer & Goldstein 2013; Horbury et al. 2018, 2020). Although they are actively studied, their origin remains an open question (Bale et al. 2019; Squire et al. 2020; Zank et al. 2020). We propose here to estimate the inertial dissipation produced by these peculiar structures in order to quantify their relative importance in the energy cascade.

We focus on a PSP1 interval on 2018 November 6 from 01:30 to 02:30, where switchbacks are numerous. The first two panels of Figure 5 again highlight a clear correlation between the velocity and the magnetic field (respectively 97%, 86%, and 90% for the radial, tangential, and normal components), which testifies to the presence of outward Alfvén waves. By following the evolution of $|\mathcal{D}_{\rm I}^{\sigma}|$ as a function of σ on switchbacks located at times $t_\star$, a power law close to $\sigma^{-3/4}$ seems to emerge. This does not correspond to any scaling laws presented in Section 2. Note that there is a zoology of nonregular fields and the fact that we find empirically a $\sigma^{-3/4}$ dependence could mean that a switchback is not strictly speaking a simple jump. However, as far as we know, the precise mathematical structure that could reproduce this σ dependence is not known. The fifth panel shows mainly a flat curve for both the mean rate of energy cascade and the inertial dissipation. We also see that the values coincide relatively well in the limit of small-scale σ. The fact that ε is relatively smooth and constant may come from the fact that the discontinuities are so large that they impose at all scales their jump (or amplitude) on the increments $\delta\boldsymbol{u}$ and $\delta\boldsymbol{b}$, which would then lead to a higher value of ε (compared to Figure 4). Although both estimates ($|\langle\mathcal{D}_{\rm I}^{\sigma}\rangle|$ and $|\varepsilon|$) give a similar result, rigorously speaking, the exact law should not be applicable in this type of data. The last panel is a 3D space-scale diagram of inertial dissipation, which highlights that switchbacks make the main contribution to the energy cascade. Indeed, one can observe that the large-scale contribution of the inertial dissipation comes from the locations where switchbacks occur, and we observe the same behavior as in Section 4.1: the dark areas mark the limit of the impact of a discontinuity on its vicinity. Overall, we observe that the values of $|\mathcal{D}_{\rm I}^{\sigma}|$ for switchbacks—particularly in the limit of small σ—are significantly higher than the values found for the other types of singularities (characterized by other power laws—see also the end of Section 2.2), which suggests that switchbacks can contribute to a stronger heating.

4.3. Statistical Results

We conclude our data analysis with a statistical comparison between the mean inertial dissipation and the mean rate of energy transfer as a function of the solar wind speed and the level of the magnetic field fluctuations. Note that the latter is estimated by the ratio between the root mean square $B_{\rm RMS}$ and the mean value B_0 of the magnetic field.

In Figure 6, we show $|\langle\mathcal{D}_{\rm I}\rangle|$ as a function of $|\varepsilon|$ for each processed interval. The upper panels correspond to THEMIS-B intervals (triangles for slow wind and squares for fast wind) and the lower panels to PSP intervals (triangles for PSP1 and squares for PSP5). The dashed (diagonal) line obeys the equation $|\langle\mathcal{D}_{\rm I}\rangle| = |\varepsilon|$. The colors in the left column reflect the mean solar wind velocity, while those in the right column correspond to the amplitude of the magnetic field fluctuations of each of the intervals. First, we notice that near the Sun (bottom panels), the values of $|\langle\mathcal{D}_{\rm I}\rangle|$ and of $|\varepsilon|$ are higher than near the Earth (top panels). This property can be attributed primarily to the strength of magnetic field, which intensifies as one approaches the Sun, but also to the omnipresence of discontinuities near the Sun. Note that the decrease of the cascade rate with the heliocentric radial distance has already been measured from exact laws or turbulence transport models (Bandyopadhyay et al. 2020; Andrés et al. 2021), but the new observation regarding $|\langle\mathcal{D}_{\rm I}\rangle|$ was achieved thanks to our inertial model that applies in the presence of discontinuities. Second, a clear correlation with the wind speed is found at 1 au with the two methods: the faster the wind, the higher the mean rate of energy transfer. This property was also shown by Hadid et al. (2017) using exact (compressible and incompressible) laws. Note that only THEMIS-B data include fast winds (PSP orbits near the Sun remain mainly in the equatorial plane where the wind is generally slow). Third, in the right column, no clear behavior emerges in the magnetic field fluctuations at 1 au, while for the PSP intervals, even if these events are few and thus statistically meaningless, large values of $B_{\rm RMS}/B_0$ tend to reduce the mean rate of energy transfer (see also Figure 9 in

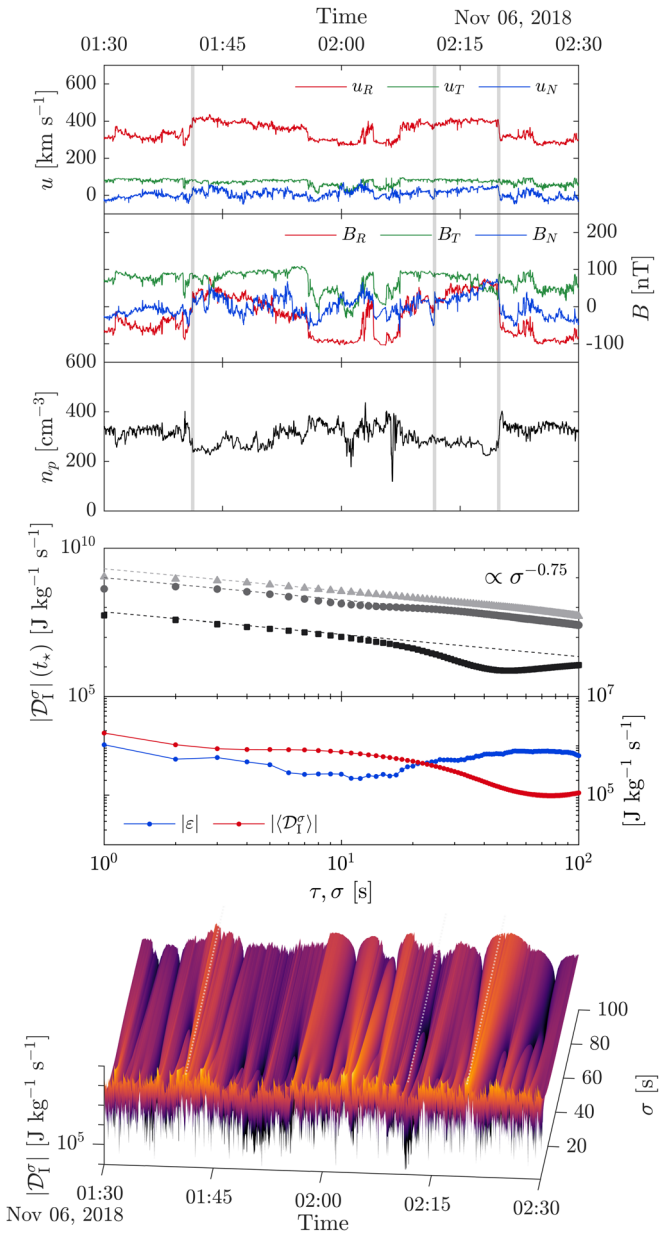

Figure 5. 1 hr interval of PSP1 with switchbacks. From top to bottom: velocity components, magnetic field components, proton density, modulus of inertial dissipation (at different times (see also the vertical gray lines in the first three panels and dotted white lines in the last one) $t_\star = \{01{:}41{:}13,\ 02{:}11{:}47,\ 02{:}19{:}53\}$ in gray, black, and light gray, respectively) as a function of σ, modulus of 1 hr-averaged inertial dissipation as a function of σ (red) and modulus of mean rate of energy cascade as a function of τ (blue), and finally the 3D map of the modulus of inertial dissipation where the color is related to the intensity and thus to the height of $|\mathcal{D}_I^\sigma|$. Velocity and magnetic fields are expressed in RTN coordinates.

Appendix B). Last, the majority of the values lies above the diagonal, meaning that on average $|\langle\mathcal{D}_I\rangle| > |\varepsilon|$. This observation can be seen as a signature of inhomogeneities (discontinuities) that are not well captured by the method using the exact law. These inhomogeneities lead mainly to a nonlocal contribution visible at large σ (see Figures 3 and 5).

5. Discussion and Conclusion

In this paper, we have used two different methods (or exact laws) to measure the rate of turbulent energy transfer at MHD

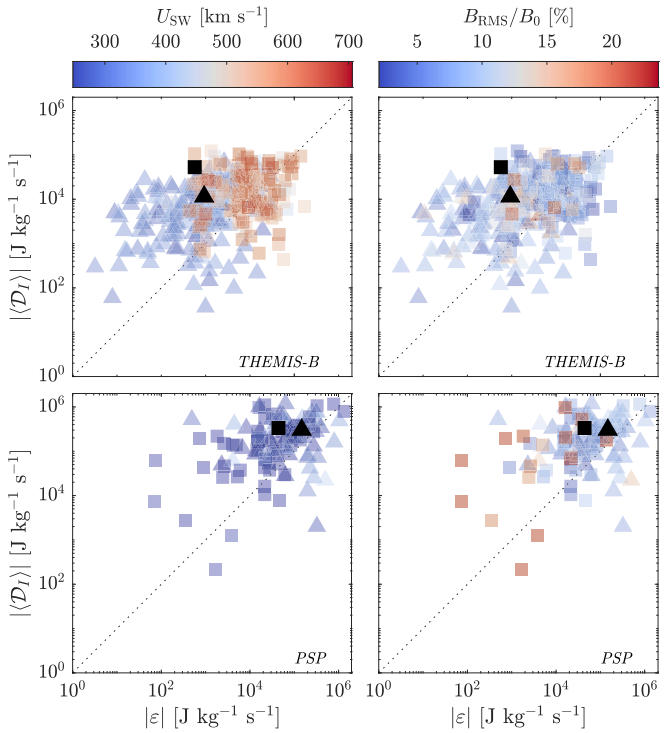

Figure 6. Inertial dissipation as a function of the mean rate of energy transfer measured via the PP98 law. The color scales correspond to the solar wind velocity (left) and to the magnetic field fluctuations (right). The triangle and square markers respectively refer to the slow and fast winds (THEMIS-B) in the upper panels, and to PSP1 and PSP5 in the lower panels. The dashed (diagonal) lines correspond to $|\langle\mathcal{D}_I\rangle| = |\varepsilon|$, and black markers are the intervals studied in Figure 3.

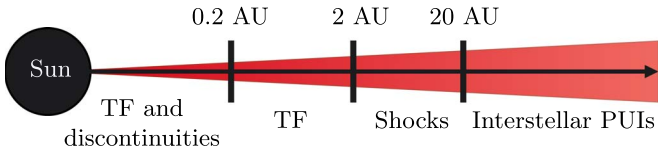

Figure 7. Overview of the observed predominant mechanisms that are responsible for the heliospheric turbulence's mean energy transfer rate. TF and PUIs stand for turbulent fluctuations and pickup ions, respectively. Note that this classification is made in terms of variations in the basic fields that enter the MHD equations. Therefore, this view is more rooted in the physics of turbulence than in the sources of turbulence of the solar wind.

scales. The first is the PP98 exact law, applicable to homogeneous turbulence, and the second is the local inertial dissipation $\mathcal{D}_I^\sigma$. Both laws have a similar form with the same combination of structure functions, but in the latter case, the homogeneity assumption is not necessary for its derivation. Therefore, $\mathcal{D}_I^\sigma$ can be considered as more general than the PP98 law since it is a local (exact) law allowing us to measure the energy transfer rate at each point of the turbulent flow even when discontinuities are present. Note that the weak formulation of the PP98 law provides a theoretical justification of the observational work of Sorriso-Valvo et al. (2018, 2019a, 2019b).

Theoretically, several scaling behaviors are expected for $\mathcal{D}_I^\sigma$ depending on the type of signals. For pure turbulent fluctuations for which the PP98 applies effectively, a flat signal is expected for $\mathcal{D}_I^\sigma$ and is reported in our study. In the presence of discontinuities, a scaling in σ^{-1} is expected and is indeed well observed over the whole available range of scales. However, no signature of a dissipation range in σ^2 is detected. These properties can be explained by the fact that the present study is limited to MHD

scales. Therefore, a natural extension of this work would be to study sub-MHD scales using data that have the required high time resolution, such as those of the Magnetospheric Multiscale mission, to see if a σ^2 dissipation can be detected. Unlike the viscous dissipation discussed in Section 2, in collisionless plasma, the dissipation involves complex physics at kinetic scales, and a variation different from σ^2 (but still with a positive slope) is likely. The method based on inertial dissipation can offer an original diagnosis to characterize this dissipation.

Inertial dissipation has many advantages over the exact law but its implementation on real data calls for some caution. This is because the dissipation formula is derived in the theoretical limit $\sigma \to 0$, which is unattainable in real data. The smallest scale that can be used in spacecraft (or simulation) data is set by the available time (or grid) resolution. To what extent the inertial dissipation estimated at this smallest *accessible* scale is representative of dissipation at the *actual* smallest scale of the system thus remains subject to caution.

The other limitation of the present study is that it is based on the MHD model. However, this limitation can (partly) be overcome by using the incompressible Hall-MHD model already derived by Galtier (2018), which would allow probing of finer scales and would possibly highlight a correlation between the inertial dissipation with temperature, or to estimate the importance of the Hall effect in the energy cascade. A further potential improvement is to account for density fluctuations and see how they would impact the inertial dissipation estimates in the solar wind. Such a model remains yet to be derived. However, even with such general models, there will always be a limitation imposed by the temporal resolution of the data that will prevent the strict application of $\sigma \to 0$.

A final caveat that should be kept in mind when estimating both the inertial dissipation and the cascade rate from the exact law, which is inherent to the use of single spacecraft data, is the validity of the Taylor hypothesis, and *even when it is valid*, how its use would impact the measured quantities. In the case of the inertial dissipation, the use of the Taylor hypothesis implies that $\mathcal{D}_{\rm I}$ only depends on a one-dimensional space variable. One can assume isotropy (as done in exact law studies) but this assumption is poorly verified in the solar wind.

Several heating mechanisms exist in the solar wind (see Figure 7) and their predominance seems to depend on the heliospheric radial distance as shown by the proton temperature measurements (with a slow decrease of the temperature up to 20 au, then an increase beyond 20 au; Matthaeus et al. 1999; Elliott et al. 2019). It is well known that around 1 au turbulent fluctuations are dominant, but closer to the Sun both discontinuities and strong turbulent fluctuations are important as now evidenced in PSP observations, while beyond 2 au we observe large-scale inhomogeneous structures such as interplanetary shocks, with relatively weak turbulent fluctuations. Beyond 20 au, the dominant heating mechanism is mainly pickup ions (Zank et al. 2018; Pine et al. 2020b). Faced with such a variety of processes, it is interesting to have a tool that allows us to quantify the turbulent energy cascade rate at fluid scales, regardless of the dominant heating mechanism at work. The inertial dissipation seems to be a good candidate for this purpose.

V.D. acknowledges B. Dubrulle for helpful discussion.

Appendix A
Comparison of Algorithms for Computation of Inertial Dissipation

To compute Equation (10), different possibilities are available. The first one, and the one chosen for this work, is to apply the gradient on the test function φ^σ. The latter being known analytically, its implementation does not introduce any numerical error and respects the hypothesis of nonregularity of the fields at the origin of the derivation of $\mathcal{D}_{\rm I}$. A second possibility is to perform an integration by part so that the gradient acts on the structure function $\boldsymbol{Y}$. The form obtained is almost identical to the PP98 law before integration, assuming isotropy, but on the one hand, this is in contradiction with the assumption of nonregularity of the fields, and on the other hand, it introduces numerical errors when computing its gradient.

To verify in practice the difference between these two computations, we compared the estimation of the inertial dissipation with and without integration by parts (hereafter named $\mathcal{D}_{\rm I}$ and $\mathcal{D}_{\rm IbP}$, respectively) as well as PP98 without the isotropy assumption, named $\varepsilon_{\rm 1D}$. In Figure 8 we show the comparison between these three methods for the interval studied in Section 4.2. The effect of the integration by part is only slightly felt at small scale because the black curve is equal to one for all of the values of σ except for the minimal one, and the gray curve confirms that when $\sigma \to \sigma_{\rm min}$, we find the equality $\langle \mathcal{D}_{\rm IbP} \rangle = \varepsilon_{\rm 1D}$ predicted theoretically.

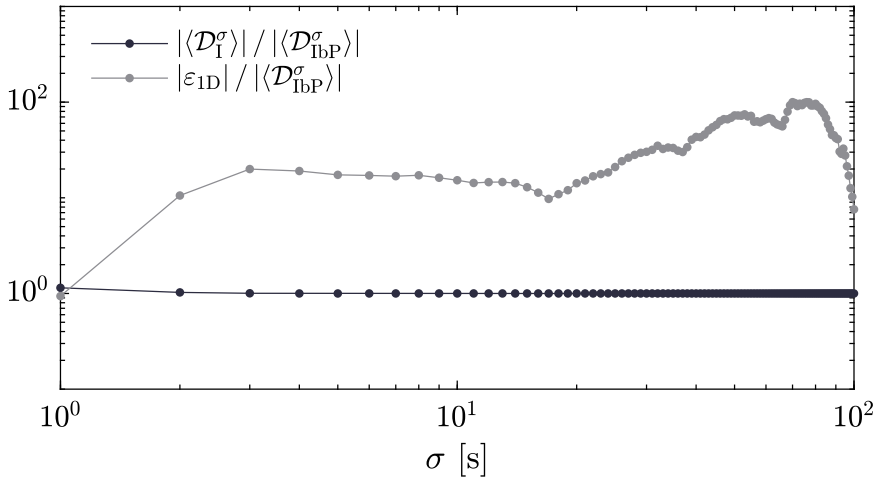

Figure 8. Evolution of $|\langle \mathcal{D}_{\rm I}^\sigma \rangle| / |\langle \mathcal{D}_{\rm IbP}^\sigma \rangle|$ and $|\varepsilon_{\rm 1D}| / |\langle \mathcal{D}_{\rm IbP}^\sigma \rangle|$ as a function of σ. For a consistent comparison, the time lag τ involved in the computation of $\varepsilon_{\rm 1D}$ takes the same values as σ.

Appendix B
Radial Evolution of the Magnetic Field

To verify that the lack of correlation underlined in the description of Figure 6 is not a curiosity, it is interesting to look at the evolution of the magnetic field as PSP approaches the Sun. Figure 9 shows that as the radial distance decreases, the average magnetic field strength B_0 increases and the ratio $B_{\rm RMS}/B_0$ decreases. This is consistent with the results of Section 4.

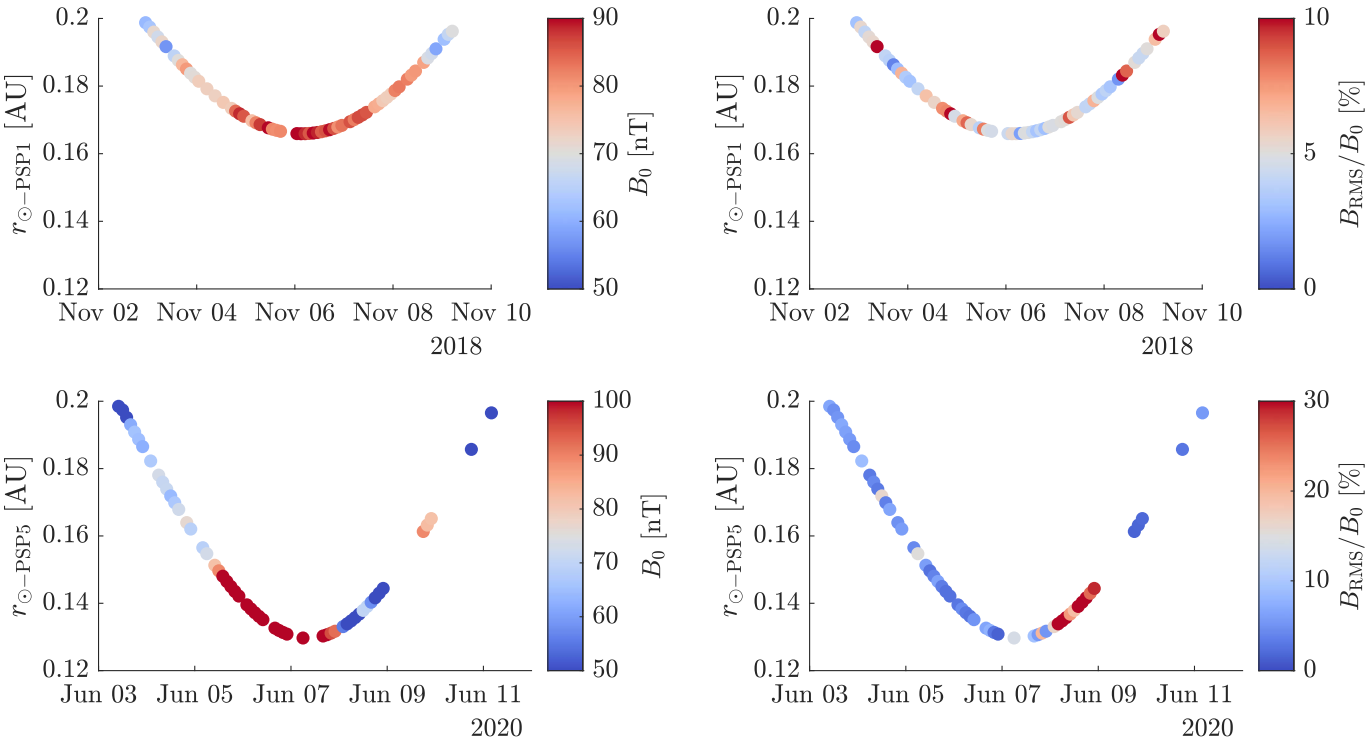

Figure 9. Radial evolution of PSP1 and PSP5 during the first (top) and fifth (bottom) approaches. The color shows the relative intensity of the average value of the magnetic field (left), and its normalized fluctuations (right).

ORCID iDs

V. David https://orcid.org/0000-0002-5013-7705
S. Galtier https://orcid.org/0000-0001-8685-9497

References

Andrés, N., Galtier, S., & Sahraoui, F. 2018, PhRvE, 97, 013204
Andrés, N., & Sahraoui, F. 2017, PhRvE, 96, 053205
Andrés, N., Sahraoui, F., Galtier, S., et al. 2019, PhRvL, 123, 245101
Andrés, N., Sahraoui, F., Hadid, L. Z., et al. 2021, ApJ, 919, 19
Antonia, R. A., Ould-Rouis, M., Anselmet, F., & Zhu, Y. 1997, JFM, 332, 395
Bale, S. D., Badman, S. T., Bonnell, J. W., et al. 2019, Natur, 576, 237
Bandyopadhyay, R., Goldstein, M. L., Maruca, B. A., et al. 2020, ApJS, 246, 48
Bandyopadhyay, R., Sorriso-Valvo, L., Chasapis, A., et al. 2020, PhRvL, 124, 225101
Banerjee, S., & Galtier, S. 2013, PhRvE, 87, 013019
Banerjee, S., & Galtier, S. 2016, JPhA, 50, 015501
Banerjee, S., Hadid, L. Z., Sahraoui, F., & Galtier, S. 2016, ApJL, 829, L27
Banerjee, S., & Kritsuk, A. G. 2017, PhRvE, 96, 053116
Banerjee, S., & Kritsuk, A. G. 2018, PhRvE, 97, 023107
Batchelor, G. K. 1953, The Theory of Homogeneous Turbulence (Cambridge: Cambridge Univ. Press)
Belcher, J. W., & Davis, L. J. 1971, JGR, 76, 3534
Burlaga, L. F., & Mish, W. H. 1987, JGR, 92, 1261
David, V., & Galtier, S. 2021, PhRvE, 103, 063217
Dubrulle, B. 2019, JFM, 867, P1
Duchon, J., & Robert, R. 2000, Nonli, 13, 249
Elliott, H. A., McComas, D. J., Zirnstein, E. J., et al. 2019, ApJ, 885, 156
Eyink, G. 2003, Nonli, 16, 137
Eyink, G. 2019, Course Notes 553.793-794: Turbulence Theory I-II (John Hopkins University), http://www.ams.jhu.edu/~eyink/Turbulence/notes.html
Federrath, C., Roman-Duval, J., Klessen, R. S., Schmidt, W., & Mac Low, M. M. 2010, A&A, 512, A81
Ferrand, R., Galtier, S., & Sahraoui, F. 2021, JPlPh, 87, 905870220
Ferrand, R., Galtier, S., Sahraoui, F., & Federrath, C. 2020, ApJ, 904, 160
Ferrand, R., Sahraoui, F., Laveder, D., et al. 2021, ApJ, 923, 122
Frisch, U. 1995, Turbulence: The Legacy of A. N. Kolmogorov (Cambridge: Cambridge Univ. Press)
Galtier, S. 2008, PhRvE, 77, 015302(R)
Galtier, S. 2016, Introduction to modern magnetohydrodynamics (Cambridge: Cambridge Univ. Press), 288
Galtier, S. 2018, JphA, 51, 205501
Galtier, S., & Banerjee, S. 2011, PhRvL, 107, 134501
Gazis, P. R., Barnes, A., Mihalov, J. D., & Lazarus, A. J. 1994, JGR, 99, 6561
Gazis, P. R., & Lazarus, A. J. 1982, GeoRL, 9, 431
Hadid, L. Z., Sahraoui, F., & Galtier, S. 2017, ApJ, 838, 9
Hellinger, P., Verdini, A., Landi, S., Franci, L., & Matteini, L. 2018, ApJL, 857, L19
Horbury, T. S., Matteini, L., & Stansby, D. 2018, MNRAS, 478, 1980
Horbury, T. S., Woolley, T., Laker, R., et al. 2020, ApJS, 246, 45
Jacques, L., Coron, A., Demanet, L., Rivoldini, A., & Vandergheynst, P. 2010, Yet Another Wavelet Toolbox, GitHub, https://github.com/jacquesdurden/yawtb
Jaffard, S. 2006, Annales de la Faculté des sciences de Toulouse : Mathématiques, Ser. 6, 15, 3
Jaffard, S., Abry, P., & Roux, S. 2009, Proc. of the GRETSI Conference
Kolmogorov, A. N. 1941, Dokl Akad Nauk SSSR, 32, 16
Kritsuk, A. G., Norman, M. L., Padoan, P., & Wagner, R. 2007, ApJ, 665, 416
Kuzzay, D., Alexandrova, O., & Matteini, L. 2019, PhRvE, 99, 053202
Lashermes, B., Roux, S. G., Abry, P., & Jaffard, S. 2008, EPJB, 61, 201
Leray, J. 1934, AcMa, 63, 193
MacBride, B. T., Smith, C. W., & Forman, M. A. 2008, ApJ, 679, 1644
Marino, R., Sorriso-Valvo, L., Carbone, V., et al. 2008, ApJL, 677, L71
Marsch, E., Schwenn, R., Rosenbauer, H., et al. 1982, JGR, 87, 52
Matthaeus, W. H., Zank, G. P., Smith, C. W., & Oughton, S. 1999, PhRvL, 82, 3444
Neugebauer, M., & Goldstein, B. E. 2013, in AIP Conf. Proc. 1539, Solar Wind 13, ed. G. P. Zank, J. Borovsky, R. Bruno et al. (Melville, NY: AIP), 46
Onsager, L. 1949, NCim, 6, 279
Osman, K. T., Wan, M., Matthaeus, W. H., Weygand, J. M., & Dasso, S. 2011, PhRvL, 107, 165001
Pine, Z. B., Smith, C. W., Hollick, S. J., et al. 2020a, ApJ, 900, 94
Pine, Z. B., Smith, C. W., Hollick, S. J., et al. 2020b, ApJ, 900, 92
Politano, H., & Pouquet, A. 1998, PhRvE, 57, R21
Richardson, J. D., Paularena, K. I., Lazarus, A. J., & Belcher, J. W. 1995, GeoRL, 22, 325
Sahraoui, F., Hadid, L., & Huang, S. 2020, RvMPP, 4, 4
Saw, E. W., Kuzzay, D., Faranda, D., et al. 2016, NatCo, 7, 12466
Simon, P., & Sahraoui, F. 2021, ApJ, 916, 49
Sorriso-Valvo, L., Carbone, F., Perri, S., et al. 2018, SoPh, 293, 10
Sorriso-Valvo, L., Catapano, F., Retinò, A., et al. 2019a, PhRvL, 122, 035102
Sorriso-Valvo, L., De Vita, G., Fraternale, F., et al. 2019b, FrP, 7, 108
Sorriso-Valvo, L., Marino, R., Carbone, V., et al. 2007, PhRvL, 99, 115001
Squire, J., Chandran, B. D. G., & Meyrand, R. 2020, ApJL, 891, L2
Stawarz, J. E., Smith, C. W., Vasquez, B. J., Forman, M. A., & MacBride, B. T. 2009, ApJ, 697, 1119
Stawarz, J. E., Smith, C. W., Vasquez, B. J., Forman, M. A., & MacBride, B. T. 2010, ApJ, 713, 920
Yanase, S. 1997, PhPl, 4, 1010
Zank, G., Matthaeus, W., & Smith, C. 1996, JGRA, 101, 17093
Zank, G. P., Adhikari, L., Zhao, L.-L., et al. 2018, ApJ, 869, 23
Zank, G. P., Nakanotani, M., Zhao, L. L., Adhikari, L., & Kasper, J. 2020, ApJ, 903, 1